MATERIALS CHEMISTRY
FRONTIERS

RESEARCH ARTICLE

View Article Online
View Journal | View Issue



Cite this: *Mater. Chem. Front.*, 2020, **4**, 555

# Tunable benzothiadiazole-based donor–acceptor materials for two-photon excited fluorescence†

Nathan R. Paisley, Christopher M. Tonge, Don M. Mayder, Kyle A. Thompson and Zachary M. Hudson *

Received 9th October 2019,
Accepted 6th December 2019

DOI: 10.1039/c9qm00627c

rsc.li/frontiers-materials

Here we describe the synthesis of eight benzothiadiazole-based D–π–A–π–D materials and evaluate their potential as imaging agents for two-photon excited fluorescence (2PEF). These compounds exhibit fluorescent emission with $\lambda_{max}$ ranging from 529 to 674 nm in toluene and quantum yields as high as 99%. Emission from the aggregated state is also examined with all species exhibiting emission from the aggregated state. Finally, three of these compounds are encapsulated within an amphiphilic water-soluble polymer and explored as imaging agents. The use of benzothiadiazole functionalized with two locked-planarity hexamethylazatriangulene (HMAT) donors was found to give red fluorescence with the highest two-photon cross-section $\sigma_2$ of 230 GM, while also exhibiting the highest photostability of the series.



## Introduction

Two-photon (2P) materials are attracting increasing attention for applications in biological imaging,[1,2] optical power limiting,[3,4] and 3D-data storage.[5,6] Factors influencing the two-photon absorption (2PA) cross-section ($\sigma_2$) of a material have also been investigated in detail, improving our ability to design compounds for 2P applications.[7,8] In two-photon excited fluorescence (2PEF) imaging, dyes with large Stokes shifts which emit within the biological transparency window (650–1350 nm) can also be excited by light with wavelengths within that range,[9,10] enabling *in vivo* imaging that is not possible with one-photon (1P) techniques.[11] In order to maximize a material's 2PA cross-section, strong charge-transfer character in the material is desirable, as well as an extended π-bridge between electron donor (D) and acceptor (A) groups.[7,8] In addition to the two-photon cross-section of a compound, for imaging applications, a high photoluminescent quantum yield ($\Phi_{PL}$), good photostability, and solubility in the imaging media are desirable.[11] A synthetic pathway that diverges late in the synthetic route can also be of benefit, allowing a broader library of compounds to be easily screened.

*trans*-Stilbene was one of the first compounds investigated for 2P properties, and stilbene derivatives are still commonly used as 2P dyes today.[8,12,13] Functionalization with hydroxy, alkoxy, or amine donors improves the $\sigma_2$ of these compounds, as well as red-shifting their emission spectra.[8] These systems often have peak emission at wavelengths shorter than 650 nm, however, achieving emission within the biological transparency window is challenging.[13] Porphyrins have been explored as 2P dyes, and take advantage of their high transition-dipole moment which can give large $\sigma_2$ values.[8,14,15] 2,1,3-benzothiadiazole (BTD) has also been investigated as a component in 2P materials and can give emission within the biological transparency window.[16–18]

The use of BTD as an acceptor unit in organic electronics is widespread, and this moiety has been used in antibacterial, organic photovoltaic, fluorescent, and thermally activated delayed fluorescence materials.[19] BTD-based compounds are typically highly stable, have a high $\Phi_{PL}$, facilitate excitation in the visible range, and exhibit large Stokes shifts in emissive derivatives.[19–21] These features make BTD intriguing as an electron-accepting core for 2P applications. Functionalization with electron-donating moieties connecting *via* a π bridge should thus yield compounds that are strongly emissive, stable, and can be excited within the biological transparency window.

Herein, we investigate a series of quadrupolar D–π–A–π–D compounds with a BTD acceptor and a range of donor moieties and examine their potential as two-photon imaging agents. These compounds exhibit fluorescent emission ranging from 529 to 674 nm with quantum yields as high as 99%. Molecular planarity has a higher effect than donor strength on the resulting $\sigma_2$ of the compounds. Finally, we investigate three of these compounds as potential water-soluble imaging agents, with the use of a locked-planarity amine donor yielding a particularly promising bright, stable system exhibiting red fluorescence.

*Department of Chemistry, The University of British Columbia, 2036 Main Mall, Vancouver, British Columbia, Canada V6T 1Z1. E-mail: zhudson@chem.ubc.ca; Fax: +1-604-822-2847; Tel: +1-604-822-3266*

† Electronic supplementary information (ESI) available. CCDC 1953988–1953990. For ESI and crystallographic data in CIF or other electronic format see DOI: 10.1039/c9qm00627c

## Results and discussion

### Synthesis

2,1,3-Benzothiadiazole (BTD) can be symmetrically modified at the **4** and **7** positions using bromination and palladium-based cross-coupling methods. We first installed a phenyl spacer as the π bridge, linking to donors with a range of electron donor strengths. These materials would then be used to form water-soluble fluorescent micelles by coprecipitation with an amphiphilic polymer, facilitating imaging in aqueous media while limiting losses in quantum yield.[22,23]

Suzuki coupling of brominated BTD **1** with phenylboronic acid gave **2** in 60% yield (Scheme 1). Following the installation of the π bridge, this compound can once again be dibrominated with $Br_2$ in the presence of $I_2$ to give **3**. This compound acts as a useful intermediate, as Buchwald–Hartwig amination can then be used to prepare a series of donor–acceptor materials by installing 9,9-dimethyl-9,10-dihydroacridine (DMAC, **4a**), phenoxazine (POZ, **4b**), phenothiazine (PTZ, **4c**), 5-methylphenazine (MPAZ, **4d**), 9′*H*-9,3′:6′,9″-tercarbazole (TCz, **4e**), or 3,6-bis(di(*p*-tolyl)aminyl)carbazole (TTCA, **4f**) groups. Due to their low solubility in the reaction medium, purification was completed by filtration of the cooled mixture to collect the solid crude product. The mixture was then dissolved in $CH_2Cl_2$ and any undissolved solids were removed by gravity filtration. Volatiles were removed *in vacuo*, yielding the target compounds in approximately 95% purity by $^1$H NMR. The compounds could then be further purified by either Soxhlet extraction or short silica column to obtain analytically-pure materials.

To target an ultra-low bandgap material, we also designed a thiophene-bridged molecule with MPAZ donors. Thiophene-bridged BTD materials are commonly used in bulk-heterojunction polymer solar cells and have been shown to significantly increase $\sigma_2$ in BTD materials.[24,25] To synthesize the thiophene-bridged species, **5** was formed from **1** by a Negishi coupling reaction using (2-thiophenyl)zinc chloride (Scheme 2). A subsequent bromination with *N*-bromosuccinimide (NBS) afforded **6** which was then amenable to the addition of MPAZ *via* a Buchwald–Hartwig amination to give **7**.

Hexamethylazatriangulene (HMAT) has also been used in 2PA systems to lock molecular planarity, resulting in high values for $\sigma_2$.[26–29] In dendritic triphenylamines, the use of HMAT instead of analogous, nonplanar triarylamines led to a 4 times increase in $\sigma_2$ between molecules with similar size and structure.[29] Due to reduced energy losses in the excited state imposed by its molecular rigidity, molecules including the HMAT donor also typically exhibit improved $\Phi_{PL}$ relative to analogous, nonplanar systems.[28,30]

Based on the demonstrated benefits of HMAT materials, a planarized version of **4a** was synthesized from 2-bromohexamethyltriangulene (HMAT-Br) to give **9** (Scheme 3). HMAT is synthesized from methyl anthranilate and methyl 2-iodobenzoate in three steps,[27] after which selective bromination with NBS yields HMAT-Br.[27] In analogy with **5**, a Negishi coupling reaction was initially attempted between **1** and HMAT-Br by formation of the organozinc chloride of HMAT, yet this reaction gave negligible amounts of compound **9**. Pinacol borane groups were therefore added to **1** *via* Suzuki coupling to give **8**, which furnished D–A–D type **9** upon Suzuki coupling.

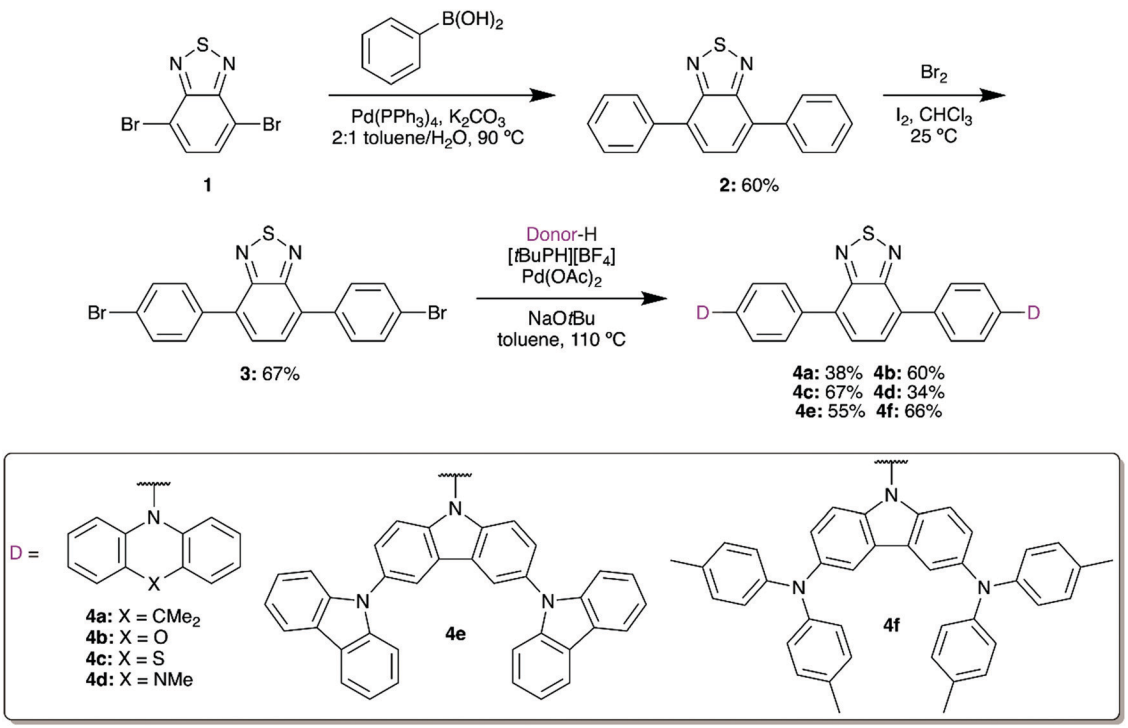


Scheme 1 Synthesis of donor–acceptor–donor benzothiadiazoles **4a–f**.

 

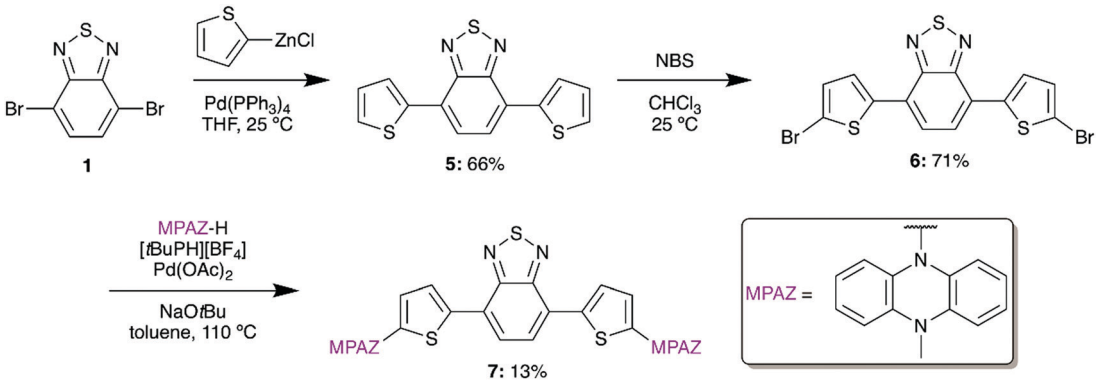


Scheme 2 Synthesis of compound **7**.

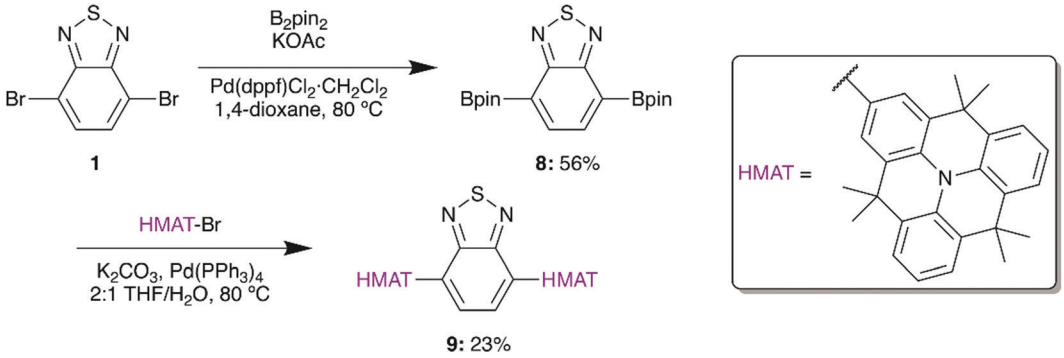


Scheme 3 Synthesis of compound **9**.



### Density functional theory calculations

Density functional theory (DFT) is useful for studying the nature of optical transitions, though DFT functionals such as B3LYP poorly describe transitions with charge-transfer character.[31–33] Range-separated hybrid (RSH) functionals such as ωB97XD better account for CT character, yet require tuning in order to optimize the functional to the specific system under study.[31,32] Hybrid functionals, such as B3LYP, use a fixed amount of exact-exchange (from Hartree–Fock theory) in addition to electron correlation (from DFT).[31] RSH functionals use a variable amount of exact-exchange and electron correlation that changes with distance according to a pre-set range separation value ($\omega$).[31] Gap tuning, for a specific molecule, can be performed on RSH functionals by varying $\omega$ to minimize the difference between the ionization potential and HOMO energy, as well as between the electron affinity and LUMO energy.[31,32] The Tamm–Dancoff approximation (TDA) scheme of time-dependant DFT (TD-DFT) discards the deexcitation matrix present in TD-DFT.[34] The advantage of using TDA-DFT over TD-DFT is in the calculation of triplet energies, saving significant computational time while still giving reliable absorption spectra.[34] This is especially beneficial for systems which suffer from the triplet instability problem, and when dealing with large molecules.[34]

With these considerations in mind, DFT calculations were run using the gap-tuned RSH functional ωB97XD (hereon denoted ωB97XD*) and the 6-31+G(d) basis set. Structures were initially optimized using ωB97XD with the default range separation value. The resulting structure was then used to gap-tune the ωB97XD functional and give a specific ωB97XD* functional for each compound. TDA-DFT calculations were run at the ωB97XD*/6-31+G(d) level in toluene using the polarizable continuum model. Natural transition orbitals (NTOs) for the $S_1$ excited state were computed to gain insight into the nature of the 1PA transition (Fig. 1). Time-dependant calculations often show multiple orbital contributions for each transition; NTOs combine these multiple transitions into ideally one particle-hole (excited state-ground state) pair. Compounds **4a–d** and **7** primarily show CT character in their respective NTOs with no significant overlap between particle and hole orbitals. **4e**, **f**, and **9** have a significant amount of π to π* character in addition to CT character with orbital contribution from the BTD core in both the particle and hole orbitals.

### Structural characterization

Solid-state molecular structures were obtained from single crystal X-ray diffraction (XRD) for **4a–c** (Fig. 2). The average BTD-phenyl dihedral angle is 27.6°, 41.9°, and 38.7° for **4a**, **4b**, and **4c**, respectively, while the average phenyl-donor dihedral angles are 77.9°, 71.8°, and 80.5°. The DMAC donor units in **4a** show significant deviation from planarity, appearing puckered about the central dimethylmethylene bridge, while the donor moieties in **4b** and **4c** are nearly planar. Molecular packing

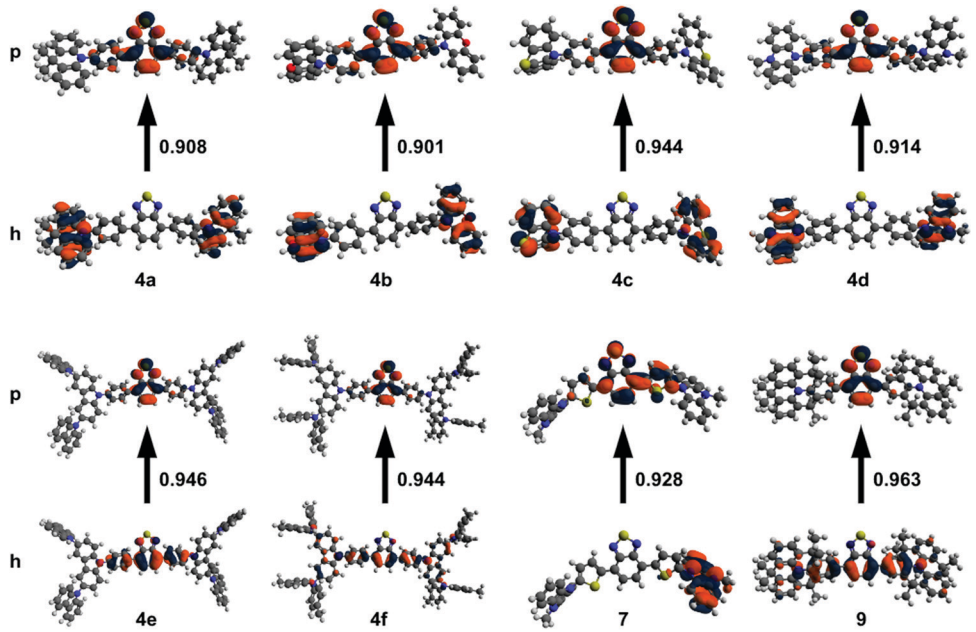


Fig. 1 NTOs for **4a–f**, **7**, and **9** showing particle–hole (p–h) pairs for the $S_0$ to $S_1$ transition. Calculated using TDA-DFT conducted at the ωB97XD*/6-31+G(d) level. The fractional contribution of the particle–hole pair to the total transition is shown between the two orbitals.

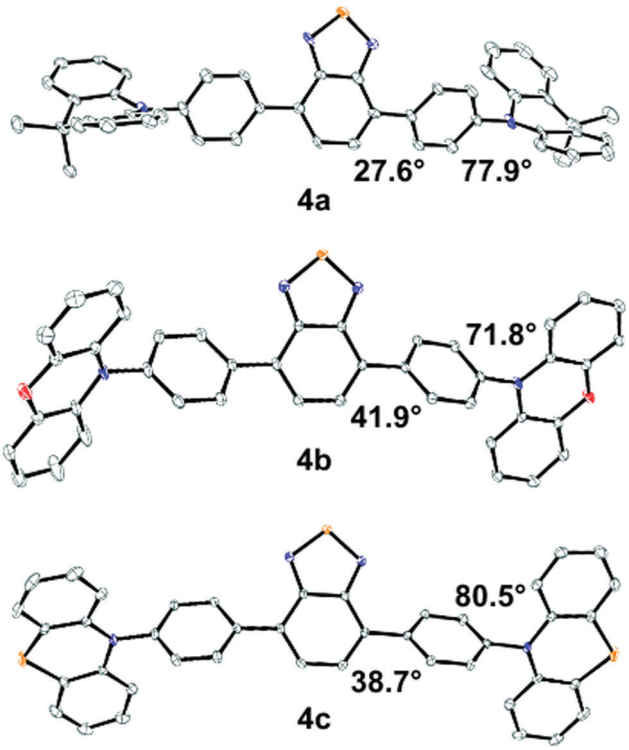


Fig. 2 Molecular structures of **4a–c** with thermal ellipsoids at the 50% probability level. Hydrogen atoms have been omitted for clarity. Carbon = grey, nitrogen = blue, oxygen = red, sulfur = yellow. Respective average BTD-phenyl and phenyl-donor dihedral angles are shown.

of **4b** shows ∼4 Å π–π stacking interactions between the POZ donor and BTD core, however, no such interactions are observed in **4a** or **4c** (Fig. S2–S4, ESI†).

The calculated structures of **4a–c** have similar BTD-phenyl dihedral angles at ∼43.3° and are larger than those determined from XRD. The phenyl-donor dihedral in **4a** is 90°, which is higher than the value determined from XRD, while the same angle in **4b** and **4c** is similar to their XRD values. The planarity of the donors in **4a–c** is opposite to the XRD structures with the DMAC donors in **4a** showing no deviation from planarity and significant puckering occurring in the POZ and PTZ donors in **4b** and **4c**, respectively. Comparing the calculated structures; **4d** has a similar BTD-phenyl and phenyl-donor dihedral as **4a–c**, and the MPAZ donor is puckered. **4e** and **4f** have similar BTD-phenyl dihedrals as **4a–c**, however, the phenyl-donor dihedral is significantly lower at 60.7° and 55.4°, respectively. **7** has a smaller BTD-thiophene dihedral of 21.7° and the thiophene-donor dihedral is similar to the analogous dihedral in **4d**. In **9** the calculated BTD-donor dihedral is substantially smaller at 39.2°, a result of the donor moiety's limited ability to twist relative to the others.

## One-photon photophysical properties

One-photon absorbance (1PA) spectra are shown in Fig. 3. The lowest energy transition for **4a–c** have respective maxima between 378 and 383 nm. **4d** has an absorbance band at 449 nm which is red-shifted from **4a–c**. The strong donor strength of the MPAZ moiety shrinks the band gap, leading to a lower energy absorbance relative to **4a–c**. **4e** and **4f** have lower-energy bands located at 401 and 440 nm, respectively, due to their increased π–π* excited state character compared to **4a–c**. **7** has an absorbance maximum at 447 nm, consistent with the extended nature of the calculated $S_1$ particle NTO. **9**, the most planar of the compounds tested, shows the most red-shifted absorption at 487 nm. Molecular conformations are

 

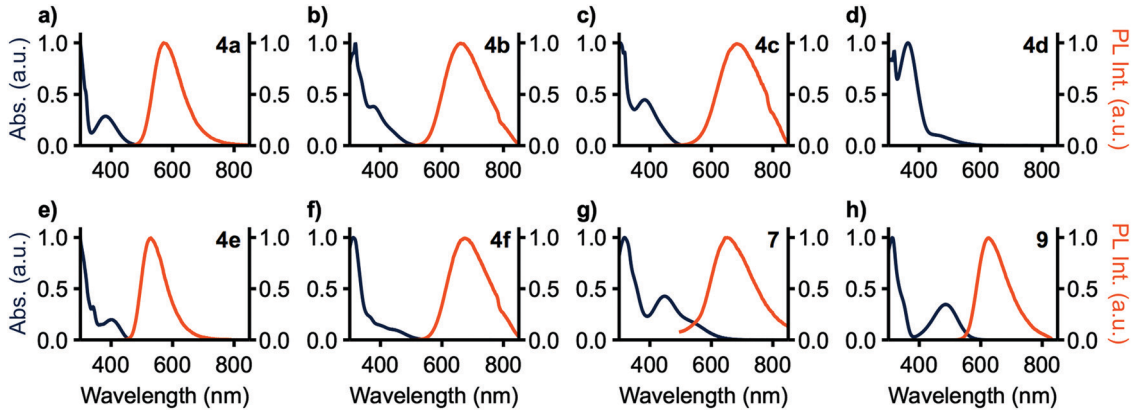


Fig. 3 Normalized one-photon absorbance (deep blue) in $CH_2Cl_2$ and photoluminescence (PL, orange) of BTD-based D–π–A–π–D and D–A–D compounds in toluene (**4a–f**, **9**) or THF (**7**) at 0.01 mg $mL^{-1}$; $\lambda_{ex} = \lambda_{max,abs}$.



Table 1 Photophysical data for **4a–c**, **e**, **f**, and **9**

| Cmpd | $\lambda_{max}^{1PA\,a}$ (nm) | $E_{gap}^{opt}/E_{gap}^{DFT\,b,c}$ (eV) | HOMO/LUMO$^{d,e}$ (eV) | $\varepsilon^a$ ($10^4$ $M^{-1}$ $cm^{-1}$) | $\lambda_{max}^{em\,f}$ (nm) | $\Phi_{air}^f/\Phi_{N2}^g$ ($\Phi_{SS}$)$^h$ | $\tau_{air}^f/\tau_{N2}^g$ (ns) |
|---|---|---|---|---|---|---|---|
| **4a** | 381 | 2.90/3.48 | −5.2/−2.3 | 1.4 | 574 | 0.43/0.60 (0.33) | 8.9/12.4 |
| **4b** | 378 | 2.94/3.37 | −5.1/−2.2 | 1.2 | 653 | 0.15/0.21 (0.03) | 6.6/8.1 |
| **4c** | 383 | 2.85/3.53 | −5.1/−2.3 | 1.5 | 674 | 0.04/0.07 (0.03) | 6.0/7.8 |
| **4d** | 363 | 3.07/3.13 | −4.5/−1.4 | 2.5 | — | — (—) | — |
| **4e** | 401 | 2.86/3.37 | −5.4/−2.5 | 1.9 | 529 | 0.97/0.99 (0.54) | 4.8/5.0 |
| **4f** | 440 | 2.52/3.10 | −5.0/−2.5 | 1.0 | 667 | 0.19/0.22 (0.12) | 5.7/6.9 |
| **7** | 447 | 2.11/2.75 | −4.6/−2.5 | 1.2 | 652 | <0.01/<0.01 (—) | 8.0/7.9 |
| **9** | 487 | 2.31/2.73 | −5.2/−2.9 | 2.0 | 626 | 0.82/0.77 (0.30) | 6.2/6.3 |

[a] Measured in $CH_2Cl_2$ at 0.01 mg $mL^{-1}$. [b] Calculated from a Tauc plot of the UV-Vis spectrum in $CH_2Cl_2$. [c] Energy corresponding to the S1 excited state from TDA-DFT at the ωB97XD*/6-31+G(d) level. [d] HOMO = $-(E_{1/2,ox} + 4.8$ eV). [e] LUMO = (HOMO + $E_{gap}^{opt}$). [f] Measured in toluene (**4a–f** and **9**) or THF (**7**) at 0.01 mg $mL^{-1}$. [g] Measured in toluene (**4a–f** and **9**) or THF (**7**) at 0.01 mg $mL^{-1}$ with 5 min $N_2$ sparging. [h] Measured as a powder. $\lambda_{ex} = \lambda_{max,abs}$.

expected to have a significant effect on both the absorptivity of these materials, as well as their two-photon cross-sections and their propensity for thermally activated delayed fluorescence (TADF). The observed values for $\varepsilon$ (Table 1) are consistent with similar phenyl-bridged BTD-based systems,[35] and the lack of TADF in these materials is attributable to the modest donor–acceptor dihedral angles.

Photoluminescence (PL) spectra are shown in Fig. 3 and photoluminescence data is summarized in Table 1. No photoluminescence was detected from **4d** in solution at room temperature, potentially a consequence of the band-gap law as MPAZ was the strongest donor tested. **7** shows no emission in toluene solution, however, in THF solution emission is detected. All observed emission bands are broad and without vibronic character. These results are consistent with TDA-DFT showing significant charge transfer in these compounds. The trend in emission maxima matches that expected from the donor strength of the compounds, with **4a** and **4e** having the weakest donors and yellow-green emission at 574 and 529 nm, respectively. **9** has an intermediate strength donor and peak emission occurs at 626 nm. **4b**, **c**, **f**, and **7** have the strongest donors and peak emission is observed at 674, 653, 667, and 652 nm, respectively. $\Phi_{PL}$ is highest with **4a** and **4e** at 43% and 97%, respectively, and drops with increasing donor strength to a minimum of less than 1% with **7**. **9**, however, breaks this trend, with a high $\Phi_{PL}$ of 83%. Emission lifetimes for all compounds range from 4.9 to 8.9 ns and are single component in nature.

Under an inert $N_2$ atmosphere, **4a–c**, **4e**, and **4f** display enhanced $\Phi_{PL}$ and longer PL lifetimes (Table 1). $\Phi_{PL}$ values increase by a maximum of 17% (**4a**) with the remaining compounds showing a much smaller increase. A similar trend is observed with PL lifetimes, with **4a** showing an increase in lifetime of 3.5 ns and **4b**, **4c**, and **4f** showing an increase of 1.5, 1.8, and 1.2 ns, respectively. **4e**, **7**, and **9** show minimal change in lifetime.

Solvatochromism was also investigated using toluene, methylene chloride, ethyl acetate, and pyridine solutions, chosen as they provide sufficient solubility to all compounds in the series. All compounds except **4c** exhibited positive solvatochromism with the highest-energy emission in toluene. **4c** includes phenothiazine donors which may adopt either pseudoaxial or pseudoequatorial conformations,[36,37] and it is likely that solvent polarity influences the distribution between the two. **4d** shows emission around 480 nm arising from donor-based transitions, yet no charge transfer emission is observed owing to the small bandgap resulting from the highly electron-rich methylphenazine donor.

Cyclic voltammetry experiments were conducted to determine $E_{HOMO}$ (Fig. 4); the results are summarized in Table 1. Reduction peaks were not well resolved in THF solution and therefore the optical bandgap was used to calculate $E_{LUMO}$. MPAZ (**4d**) exhibits the highest HOMO energy of approximately

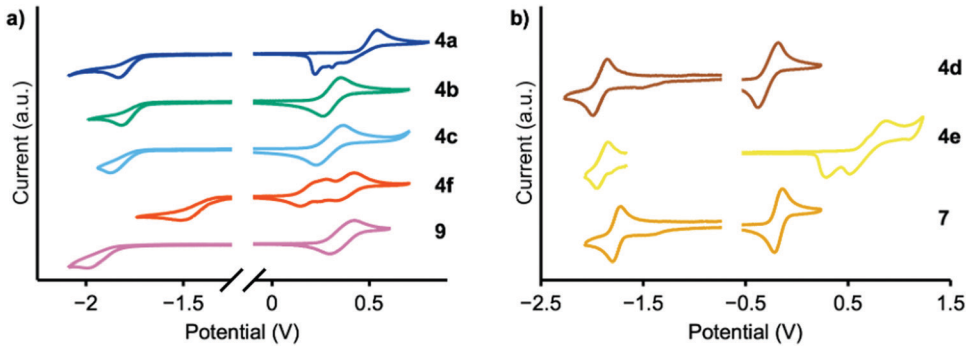


Fig. 4 Cyclic voltammograms of **4a–f**, **7**, and **9** relative to $Fc^{0/+}$, recorded at a rate of 50 mV $s^{-1}$ in THF (a, **4a–c**, **f**, and **9**) or *o*-dichlorobenzene (b, **4d**, **e**, and **7**) containing 0.001 M analyte and 0.2 M tetrabutylammonium hexafluorophosphate as the supporting electrolyte.



−4.5 eV, while the weakest donors, DMAC and TCz (**4a** and **4e**), exhibit HOMO energies of −5.2 and −5.4 eV, respectively, consistent with the expected trend in donor strength. Faradaic events occurring at potentials higher than $E_{HOMO}$ were also observed and likely correspond to electrodeposition, electropolymerization events, or oxidation of the second donor moiety.

For applications in biological imaging, dissolution of these nonpolar fluorophores in aqueous environments will inevitably result in aggregation. We thus investigated the emission of each of these materials in the aggregated state by collecting spectra of each compound in THF/water solutions with $f_w$ (water fraction, v/v%) ranging from 0% to 90% (Fig. 5). **4a–c**, **e**, **f**, **7**, and **9** show emission in the aggregated state with **4f** increasing in intensity by 3400% at 90% $H_2O$. **7** shows aggregation-caused quenching behaviour. The remaining compounds emit in $f_w$ 0% solutions, then drop in emission intensity as $f_w$ increases before again rising in intensity at high water fraction. At a $f_w$ of 90%, **4a**, **4b**, and **4e** emit with slightly higher intensity compared to their emission in pure THF, while **4c** and **9** are lower in intensity at $f_w$ = 90%. In THF solution **4b** and **4c** show strongly blue-shifted emission, relative to their emission at $f_w$ above 60%, possibly arising from donor-based transitions (POZ and PTZ, respectively). **4c** also shows dual emission below $f_w$ 60%. This is consistent with previous studies showing that PTZ has multiple emissive conformations.[38,39] The mechanism for emission enhancement in **4a–f** is likely due to restriction of vibrational motion within the donor, as well as restricted rotational motion about the phenyl spacers.[35,40] At high $f_w$ aggregation of the materials is expected to reduce intramolecular motion, consistent with reduced non-radiative relaxation.

Solid-state quantum yields were determined to further investigate the effects of aggregation (Table 1). All compounds except **4d** are emissive in the solid state but with reduced $\Phi_{PL}$ compared to their solution values. The largest decrease is observed for **4b** and **9**, resulting in $\Phi_{PL}$ of 3% and 30% compared to 15% and 82%, respectively, in toluene solution. In the molecular structure of **4b**, significant π stacking interactions are observed which led to increased quenching over **4a** and **4c**.

### Two-photon excited fluorescence

The two-photon cross-sections ($\sigma_2$) of all emissive compounds were determined using the two-photon excited fluorescence (2PEF) method from 710 to 980 nm, the limits of our laser.[41] Rhodamine 6G in MeOH was used as the reference for all samples. Samples were periodically checked to ensure a square dependence of signal intensity with excitation power. As shown in Fig. 6, **4a–c** and **7** display small $\sigma_2$ values. The maximum 2PA cross-section for **4c** and **7** occurs at 710 nm, the lowest wavelength tested, suggesting that the maximum $\sigma_2$ value for these compounds may occur at shorter wavelength. This may also be the case for **4a** and **4b** as they are structurally similar to **4c** with nearly identical 1PA maxima. **4e** and **4f** have improved cross-sections, with peak $\sigma_2$ values of 70 and 100 GM at 740 and 840 nm, respectively. **9** has the highest two-photon response with a maximum of 230 GM at 850 nm. **4e**, **f**, and **9** have lowest energy 2PA bands at an energy higher than their corresponding lowest energy 1PA band, consistent with studies on similar molecules.[18] This can be explained in light of the symmetry selection rules for 2PA. 2PA symmetry selection rules are opposite to those for 1PA in centrosymmetric systems, resulting in the lowest 1PA band being 2PA forbidden. While the tested molecules are not centrosymmetric, reduction in the 2PA band matching the low-energy 1PA maximum band has been previously observed for quadrupolar linear molecules such as these.[8]

The two-photon response of these compounds can be rationalized by considering the planarity of their structure. **4a–c** have large BTD-spacer and spacer-donor dihedral angles which limits their ability to undergo 2PA. **7** has a low BTD-thiophene dihedral, however, the thiophene-donor dihedral is large. **4e** and **4f** are relatively planarized with smaller spacer-donor dihedrals and **9** is further planarized with only a BTD-donor dihedral. This is consistent with studies of BTD and HMAT-derived systems finding that 2P activity scaled with the planarity of the molecule overall.[18,27,28]

We next explored the use of compounds **4e**, **f**, and **9** as fluorescent dyes encapsulated in water-soluble micelles, to explore their utility for applications in imaging. Such micelles, also known as polymer dots (Pdots), are emerging as a useful class of materials for nanoparticle-based sensing and analysis.[42–44] A high density of chromophores can be encapsulated within Pdots, offering high signal-to-noise in imaging, and functionalization with binding groups or therapeutic cargo affords multifunctional probes. **4e**, **f**, and **9** were chosen as they have the highest two-photon brightness ($\sigma_2\Phi_{PL}$) of the compounds

 

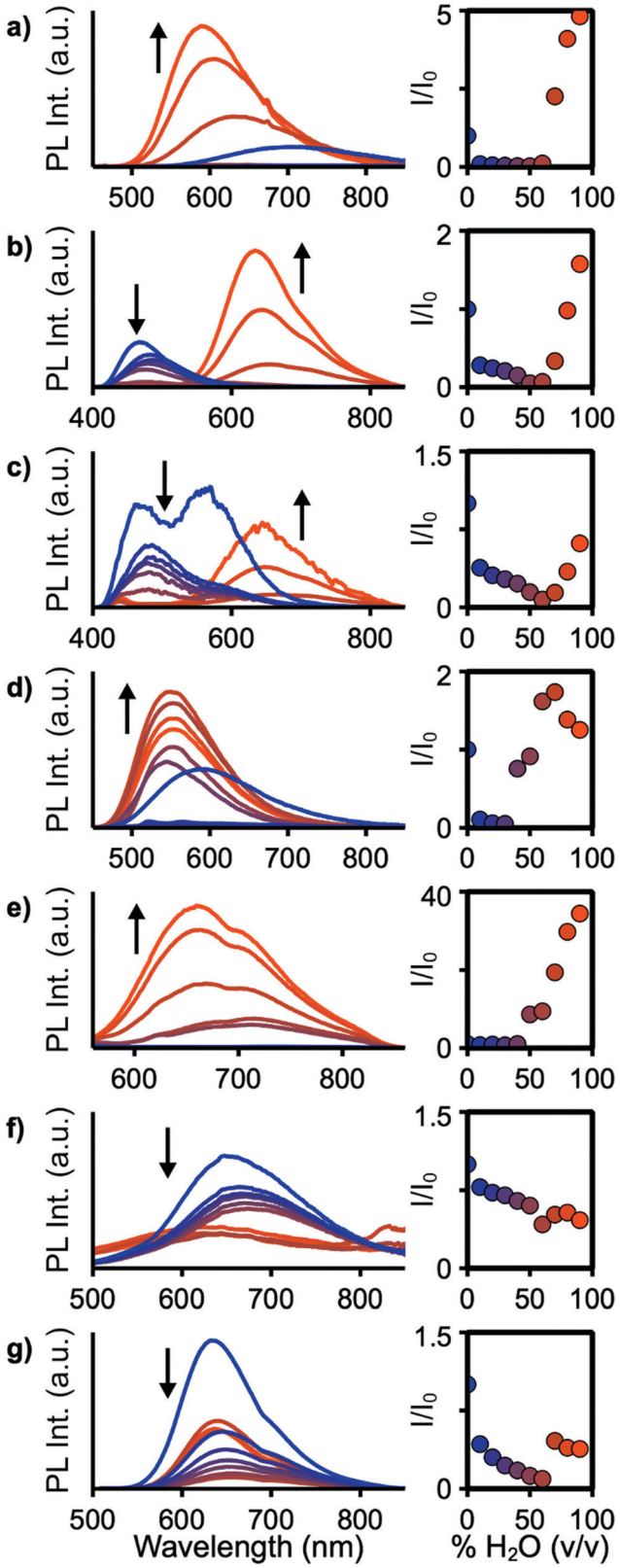


Fig. 5 Emission spectra (left) and $I/I_0$ *vs.* water fraction (right) of **4a** (a), **4b** (b), **4c** (c), **4e** (d), **4f** (e), **7** (f), and **9** (g) at concentrations of 0.01 mg mL$^{-1}$ in THF/water mixtures with $f_w$ ranging from 0% (blue) to 90% (orange).

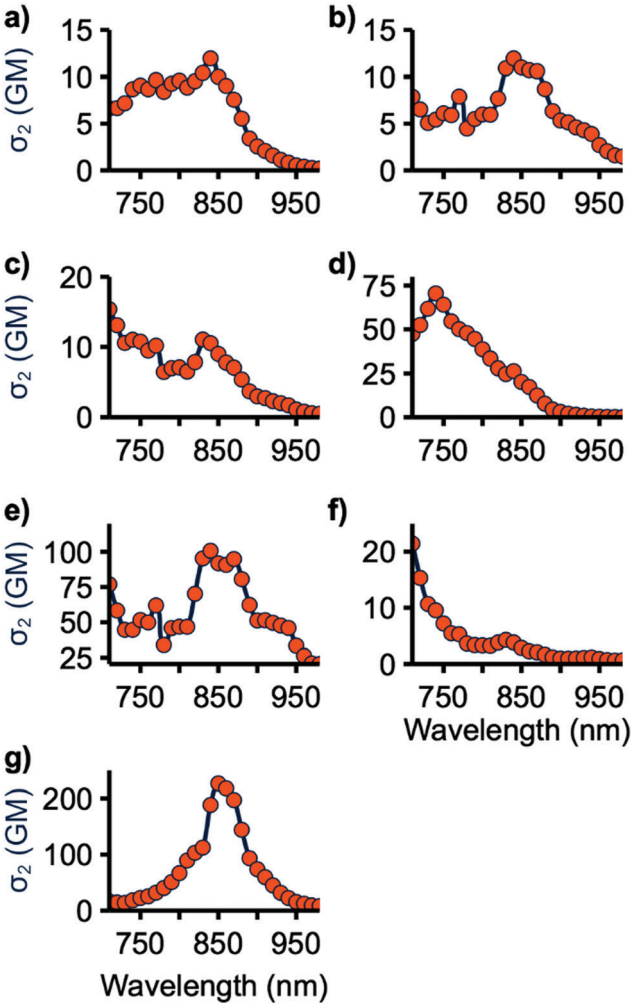


Fig. 6 Two-photon excitation spectra of **4a** (a), **4b** (b), **4c** (c), **4e** (d), **4f** (e), **7** (f), and **9** (g). Measurements were obtained every 10 nm (orange circles) using the 2PEF method. A connecting curve is provided as a visual aid. 1 GM (Göppert-Mayer) = $10^{-50}$ cm$^4$ s photon$^{-1}$.

studied. Encapsulation was performed by dissolving both the dye and the amphiphilic polymer Pluronic F127 ($PEO_{100}$-*b*-$PPO_{65}$-*b*-$PEO_{100}$) in $CHCl_3$, removing all volatiles *in vacuo*, and then redissolving the solid with sonication in water (Fig. 7a, PEO = poly(ethylene oxide), PPO = poly(propylene oxide)). The low-energy 1PA absorption maxima of these micelles is red-shifted in all cases from those of the unencapsulated dyes, with $\lambda_{max}$ = 412, 445, and 507 nm for **4e**, **f**, and **9** (Fig. 7c). The emission of **4e** and **4f** red-shift slightly to 543 and 674 nm, respectively; the emission of **9**, however, remains essentially unchanged. $\Phi_{PL}$ is reduced to 0.44, 0.05, and 0.39 for **4e**, **f**, and **9** upon encapsulation. As a representative sample, the micelles of **9** were found to have an average diameter of 129 ± 4 nm by nanoparticle tracking analysis, which also showed a monomodal particle distribution with a size dispersity of 2.9 (Fig. 7d).

The relative photostability of each micelle sample was also examined by photobleaching experiments. Each micelle sample was continuously illuminated with 450 nm light under a fluorescence microscope and emission intensity was recorded at 1 minute

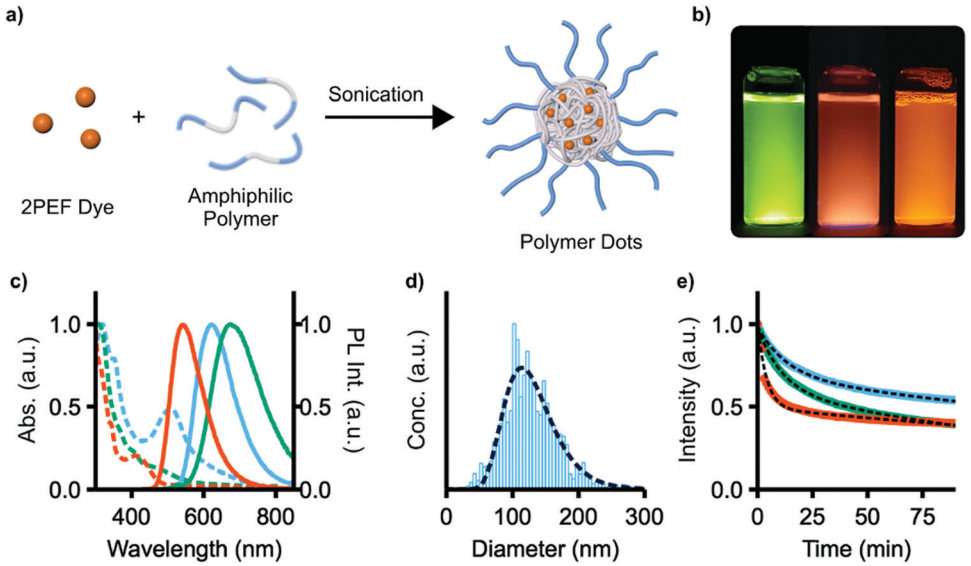


Fig. 7 (a) Encapsulation of 2PEF dyes **4e**, **4f**, or **9** in the amphiphilic polymer Pluronic F127 to produce water-soluble polymer dots. (b) **4e**, **f**, and **9**, respectively, in F127 excited with 365 nm light in water at 0.01 mg $mL^{-1}$. (c) Normalized absorbance (dashed) and photoluminescence (PL, solid) of **4e** (orange), **f** (green), and **9** (blue) in Pluronic F127 in water at 0.01 mg $mL^{-1}$. (d) Size distribution of polymer dots of **9** in aqueous solution (blue) and curve fit (dashed line) at 0.25 μg $mL^{-1}$. (e) Photobleaching of **4e** (orange), **f** (green), **9** (blue) in Pluronic F127 in water at 0.01 mg $mL^{-1}$, and exponential fit for each (dashed line).

intervals (Fig. 7e). Photobleaching occurs with two first-order rate constants of 0.25 and 0.002 $min^{-1}$, 0.09 and 0.005 $min^{-1}$, and 0.07 and 0.003 $min^{-1}$ for **4e**, **f**, and **9**, respectively. The two constants are attributed to photobleaching of the dye and the increasing penetration of excitation light into the micelles as photobleaching occurs.

## Conclusion

In this study, 8 new D–π–A–π–D type benzothiadiazoles were synthesized using a divergent synthetic pathway allowing for the facile installation of a series of donor moieties. All except **4d** are fluorescent in solution with emission maxima ranging from 529 to 674 nm and quantum yields as high as 99%. Emission from the aggregated state was also examined, with all but **4d** showing emission from the aggregated state and **4f** exhibiting a 34-fold increase in photoluminescence intensity in 90% water/THF compared to pure THF solution. 2PEF activity was also examined for this series of materials, with peak $\sigma_2$ values ranging from 12 to 230 GM. Molecular planarity was found to be the major factor affecting two-photon cross-section, with **4a–c** having the lowest $\sigma_2$ values, **4e** and **4f** having intermediate $\sigma_2$ values, while the use of HMAT as the donor with no phenyl π bridge gives the highest $\sigma_2$. Water-soluble micelles applicable to biological imaging were also formed with **4e**, **f**, or **9** encapsulated within. Photobleaching experiments revealed that **9** was significantly more stable under illumination than the other dyes examined, while still exhibiting a high quantum yield of 39% in aqueous solution. Overall, this work develops a detailed understanding of the photophysics of benzothiadiazole-based materials for two-photon imaging, with promise for applications in imaging in the biological transparency window.

## Experimental

### General considerations

All reactions were performed under a nitrogen atmosphere using standard Schlenk techniques unless otherwise stated. Solvents were of reagent grade or higher. Toluene was obtained from Caledon Laboratories, dried using an Innovative Technologies Inc. solvent purification system, collected under vacuum, and stored under a nitrogen atmosphere. All reagents were purchased from Sigma-Aldrich or Oakwood Chemical and used as received unless otherwise stated. 4,7-Dibromo-2,1,3-benzothiadiazole,[45] 4,7-diphenyl-2,1,3-benzothiadiazole,[46] 4,7-bis(4-bromophenyl)-2,1,3-benzothiadiazole,[46] 4,7-bis(2-thienyl)-2,1,3-benzothiadiazole,[45] 4,7-bis(5-bromothiophen-2-yl)-2,1,3-benzothiadiazole,[47] 4,7-bis(4,4,5,5-tetramethyl-1,3,2-dioxaborolan-2-yl)-2,1,3-benzothiadiazole,[48] 9,9-dimethyl-9,10-dihydroacridine,[49] 5-methylphenazine,[50] 9′*H*-9,3′:6′,9″-tercarbazole,[51] *N*3,*N*3,*N*6,*N*6-tetra-*p*-tolyl-9*H*-carbazole-3,6-diamine,[52] and 2-bromo-4,4,8,8,12,12-hexamethyl-8,12-dihydro-4*H*-benzo[9,1]quinolizino[3,4,5,6,7-*defg*]-acridine[53] were synthesized according to literature methods. $^{1}H$ and $^{13}C\{^{1}H\}$ nuclear magnetic resonance (NMR) spectra were measured on Bruker Avance 400 MHz or Bruker AV III HD 400 MHz spectrometers with chloroform-d ($CDCl_3$), dichloromethane-$d_2$ ($CD_2Cl_2$), tetrahydrofuran-$d_8$ (THF-$d_8$), dimethyl sulfoxide-$d_6$ (DMSO-$d_6$), or pyridine-$d_5$ (Py-$d_5$) as the solvent. Mass spectra were recorded on a Kratos MS-50 instrument using electron impact ionization or field desorption.

### Photophysical characterization

Absorbance measurements were made on a Cary 60 spectrometer with dichloromethane ($CH_2Cl_2$) as the solvent. One-photon excited fluorescence measurements were made on an Edinburgh

 

Instruments FS5 Spectrofluorometer or Cary Eclipse Fluorescence Spectrophotometer. The excitation wavelength ($\lambda_{ex}$) of all fluorescence measurements was matched to the maximum of the lowest energy absorption band determined from UV-Vis. Steady state fluorescence measurements were conducted at 10 μg mL$^{-1}$ in toluene, methylene chloride, ethyl acetate, or pyridine. Absolute photoluminescence quantum yield (PLQY) was determined using an Edinburgh Instruments SC-30 integrating sphere module. PLQY measurements were conducted in toluene at 5 μg mL$^{-1}$ (optical density at the excitation wavelength between 0.05 and 0.15). Time-correlated single photon counting (TCSPC) measurements were made on an Edinburgh Instruments FS5 Spectrofluorometer equipped with a 313 nm picosecond pulsed diode LED. Aggregation-induced emission (AIE) measurements were conducted in THF/water mixtures at 0.01 mg mL$^{-1}$. Two-photon cross-sections ($\sigma_2$) were calculated using the two-photon excited fluorescence method.[41] Two-photon cross-section ($\sigma_2$) values from 710–980 nm were measured with an inverted two-photon fluorescence scanning microscope (Zeiss LSM 510 MP). Samples (3 mL) were measured in quartz cuvettes and concentrations were adjusted to give similar 2PEF intensities (**4a**, 0.01 mg mL$^{-1}$; **4b**, 0.05 mg mL$^{-1}$; **4c**, 0.20 mg mL$^{-1}$; **4e**, 0.01 mg mL$^{-1}$; **4f**, 0.01 mg mL$^{-1}$; **7**, 1.0 mg mL$^{-1}$; **9**, 0.01 mg mL$^{-1}$ in toluene) and Rhodamine 6G in MeOH (0.001 mg mL$^{-1}$ in MeOH) was used as the ref. 41. The cuvette was illuminated at a depth of 0.6 mm from the bottom of the cuvette and imaged with a 10×/0.3 objective lens and femtosecond laser with a tuning range of 710–980 nm. The dichroic mirror had a cut-off at 660 nm and detector wavelength sensitivity was corrected for using either a 550/40 or 610/20 bandpass filter (center wavelength and bandwidth in nm). The square-dependence of the fluorescence intensity on laser power was periodically confirmed for all measured and $\sigma_2$ was calculated using the quantum yield obtained from one-photon excitation experiments.

### Photobleaching

Photobleaching measurements were done on an inverted microscope. Sample aliquots (5 μL) were measured in a clear flat-bottom 1536-well plate (Greiner Bio One, Kremsmünster, Austria) with the wells covered with universal optical sealing tape (#6575, Corning). Sample concentrations were adjusted to obtain similar initial fluorescence intensities (**4e**, 0.005 mg mL$^{-1}$; **4f**, 0.05 mg mL$^{-1}$; **9**, 0.002 mg mL$^{-1}$). A 2 × 2 array of wells was illuminated and imaged with a 4× objective lens (NA 0.16). The excitation filter was 450/50 (center wavelength and bandwidth in nm), the dichroic mirror had a cut-off at 565 nm, and the emission filter was a longpass filter with a 570 nm cut-off (Chroma, Bellows Falls, VT). The excitation power was estimated to be ~62 mW at the sample. Samples were continuously illuminated using the above conditions and images were acquired at 1 min intervals for 90 min and analyzed using ImageJ software (NIH, Bethesda, MD) with the Time Series Analyzer V3 plugin. The initial intensity for each sample was normalized to a value of unity. Photobleaching rates were determined by fitting the intensity *versus* time data with a biexponential decay function.

### Nanoparticle tracking analysis

Size and molar concentration of Pluronic F127 encapsulated **9** was determined by nanoparticle tracking analysis (NTA) using a NanoSight NS300 (Malvern Panalytical, Malvern, UK). The sample was diluted with filtered (0.22 μm) water prior to measurements (0.25 μg mL$^{-1}$). Measurements were recorded in scattering (no filter) mode using a laser wavelength of 488 nm. Nanoparticle sizes and concentrations were determined by using the NanoSight NTA software (ver. 3.3).

### Electrochemical methods

Cyclic voltammograms were recorded using a CH Instruments 660D potentiostat at room temperature using a standard three-electrode configuration (working electrode: 2 mm diameter Pt disc; reference electrode: RE-5B Ag/AgCl electrode in saturated aqueous KCl (BASi Inc.), referenced externally to ferrocene/ferrocenium; counter electrode: Pt wire) in 0.2 M tetrabutylammonium hexafluorophosphate in tetrahydrofuran or *o*-dichlorobenzene. Experiments were run at a scan rate of 50 mV s$^{-1}$ in dry degassed electrolyte solution with 0.001 M analyte.

### Density functional theory

Quantum-mechanical calculations were performed using the Gaussian 16 Rev. B.01 computational package using default settings unless otherwise stated. All geometries were optimized to a minimum, and frequency calculations were performed at the same level of theory to verify the absence of imaginary frequencies. Initial geometry optimizations were conducted at the ωB97XD/6-31+G(d) level. The optimal range-separation value ($\omega$) was determined based on the ωB97XD/6-31+G(d) level and are listed in Table S1 (ESI†). To optimize $\omega$, $J^2$ (eqn (1)) was minimized.[32] $\varepsilon_{HOMO}$ is the energy of the HOMO. IP is the ionization potential and is calculated using eqn (2). $E_{gs}$ is the energy of the ground state system.

$$J^2 = \sum_{i=0}^{1}[\varepsilon_{HOMO}(N+i) + IP(N+i)]^2 \quad (1)$$

$$IP(N) = E_{gs}(N-1) - E_{gs}(N) \quad (2)$$

Single-point energy calculations were carried out on the $N$ and $N \pm 1$ electron systems and optimization was conducted using a golden section search implemented with a bash script to find the minimum of $J^2$ and give the optimized functional (referred to as ωB97XD*). Possible $\omega$ values for the minimization were limited between 0.05 and 0.5 Bohr$^{-1}$. A second geometry optimization at the ωB97XD*/6-31+G(d) level was conducted. Vertical excitation (absorption) energies of the lowest singlet- and triplet-excited states were calculated using the Tamm–Dancoff approximation (TDA) scheme of time-dependent DFT (TD-DFT) at the ωB97XD*/6-31+G(d) level in toluene using the polarizable continuum model (PCM). Natural transition orbitals (NTOs) were calculated using Multiwfn Version 3.6.

### X-ray crystallography

Single yellow plate-shaped (**4a**), orange prism-shaped (**4b**), or red needle-shaped (**4c**) crystals were recrystallized from a

mixture of THF and heptane by slow evaporation. A suitable crystal (0.40 × 0.30 × 0.03) mm$^3$ (**4a**), (0.28 × 0.26 × 0.14) mm$^3$ (**4b**), or (0.54 × 0.11 × 0.06) mm$^3$ (**4c**) was selected and mounted on a mylar loop in oil on a Bruker APEX II area detector diffractometer. The crystal was kept at a steady $T$ = 90(2) K during data collection. The structure was solved with the XT[54] structure solution program using the Intrinsic Phasing solution method and by using Olex2[55] as the graphical interface. The model was refined with version 2018/3 of XL[56] using Least Squares minimization CCDC 1953988–1953990.†

### General reaction A

Carried out using a modified literature method.[57] An oven-dried 100 mL 3-neck round-bottom flask was equipped with a liquid-cooled condenser, Teflon stir bar, glass stopper, and rubber septum. The flask was evacuated and back filled with nitrogen gas three times. **3** (1.12 mmol, 500 mg, 1 eq.), [*t*-Bu$_3$PH][BF$_4$] (0.13 mmol, 39 mg, 0.12 eq.), palladium(II)acetate (0.06 mmol, 13 mg, 0.05 eq.), sodium *tert*-butoxide (2.8 mmol, 269 mg, 2.5 eq.) and the respective donor (2.7 mmol, 2.4 eq.) were added rapidly to the flask under positive nitrogen gas flow. The flask was again evacuated and back filled with nitrogen gas three times. Toluene (23 mL) was added *via* air-tight syringe and the reaction was heated to reflux with an oil bath set to 130 °C. The reaction was monitored by TLC (1 : 1 hexanes : dichloromethane) until no **3** remained. The reaction was cooled to room temperature. The precipitated product was isolated by vacuum filtration and rinsed with a minimal amount of cold toluene. The collected solid was dissolved in dichloromethane and filtered by gravity. Volatiles were removed from the filtrate to isolate the solid product.

**4,7-Bis(4-(9,9-dimethylacridin-10(9*H*)-yl)phenyl)-2,1,3-benzothiadiazole (4a).** Synthesized according to general reaction A with DMAC as the donor. Product isolated as a bright yellow powder (298 mg, 38%). $^1$H NMR (400 MHz, THF-d$_8$): $\delta$ 8.43 (d, $J$ = 8.4 Hz, 4H), 8.14 (s, 2H), 7.54 (d, $J$ = 8.4 Hz, 4H), 7.48 (dd, $J$ = 7.7, 1.6 Hz, 4H), 6.92 (dtd, $J$ = 26.0, 7.3, 1.5 Hz, 8H), 6.41 (dd, $J$ = 8.1, 1.4 Hz, 4H), 1.69 (s, 12H). $^{13}$C{$^1$H} NMR (101 MHz, THF-d$_8$): $\delta$ 154.83, 142.33, 141.73, 138.00, 133.25, 132.50, 132.04, 130.78, 129.13, 126.90, 125.72, 121.23, 114.76, 36.59, 31.30. HRMS (EI-TOF) $m/z$: M$^{\bullet+}$ calculated for [C$_{48}$H$_{38}$N$_4$S]$^{\bullet+}$ 702.2817; found 702.2806; difference −1.53 ppm.

**4,7-Bis(4-(10*H*-phenoxazin-10-yl)phenyl)-2,1,3-benzothiadiazole (4b).** Synthesized according to general reaction A with POZ as the donor. The initially isolated solid was further purified with a silica plug (1 : 1 hexanes : dichloromethane). Product isolated as an orange/red powder (437 mg, 60%). $^1$H NMR (400 MHz, THF-d$_8$): $\delta$ 8.40 (d, $J$ = 8.4 Hz, 4H), 8.10 (s, 2H), 7.57 (d, $J$ = 8.4 Hz, 4H), 6.71–6.57 (m, 12H), 6.08 (dd, $J$ = 7.1, 2.2 Hz, 4H). $^{13}$C{$^1$H} NMR (101 MHz, THF-d$_8$): $\delta$ 154.78, 144.83, 140.05, 138.27, 135.12, 133.19, 132.72, 131.53, 129.13, 123.93, 122.00, 115.96, 114.09. HRMS (EI-TOF) $m/z$: M$^{\bullet+}$ calculated for [C$_{42}$H$_{26}$N$_4$O$_2$S]$^{\bullet+}$ 650.1776; found 650.1767; difference 0.61 ppm.

**4,7-Bis(4-(10*H*-phenothiazin-10-yl)phenyl)-2,1,3-benzothiadiazole (4c).** Synthesized according to an altered general reaction A with PTZ as the donor, using **3** (0.45 mmol, 200 mg, 1 eq.), [*t*-Bu$_3$PH][BF$_4$] (0.05 mmol, 15 mg, 0.12 eq.), palladium(II)acetate (0.02 mmol, 5 mg, 0.05 eq.), sodium *tert*-butoxide (1.12 mmol, 108 mg, 2.5 eq.), PTZ (1.08 mmol, 214 mg, 2.4 eq.), and toluene (9 mL). The initially isolated solid was further purified with a silica plug (1 : 1 hexanes : dichloromethane). Product isolated as an orange/red powder (206 mg, 67%). $^1$H NMR (400 MHz, THF-d$_8$): $\delta$ 8.38 (d, $J$ = 8.5 Hz, 4H), 8.09 (s, 2H), 7.58 (d, $J$ = 8.5 Hz, 4H), 7.05 (dd, $J$ = 7.5, 1.7 Hz, 4H), 6.96–6.81 (m, 8H), 6.46 (dd, $J$ = 8.1, 1.3 Hz, 4H). $^{13}$C{$^1$H} NMR (101 MHz, THF-d$_8$): $\delta$ 154.81, 144.94, 142.35, 137.51, 133.12, 132.27, 130.54, 129.01, 127.52, 127.38, 123.41, 122.18, 117.65. HRMS (EI-TOF) $m/z$: M$^{\bullet+}$ calculated for [C$_{42}$H$_{26}$N$_4$S$_3$]$^{\bullet+}$ 682.1320; found 682.1286; difference −4.91 ppm.

**4,7-Bis(4-(10-methylphenazin-5(10*H*)-yl)phenyl)-2,1,3-benzothiadiazole (4d).** Synthesized according to general reaction A with MPAZ as the donor. Product isolated as a dark red powder (261 mg, 34%). $^1$H NMR (400 MHz, pyridine-d$_5$): $\delta$ 8.46 (d, $J$ = 7.9 Hz, 4H), 8.08 (s, 2H), 7.65 (d, $J$ = 8.0 Hz, 4H), 6.80 (t, $J$ = 7.6 Hz, 4H), 6.59 (t, $J$ = 7.6 Hz, 4H), 6.49 (d, $J$ = 7.8 Hz, 4H), 6.16 (d, $J$ = 7.8 Hz, 4H), 2.95 (s, 6H). $^{13}$C{$^1$H} NMR (101 MHz, pyridine-d$_5$): $\delta$ 154.78, 141.60, 139.14, 138.04, 137.68, 133.12, 132.99, 131.34, 129.31, 122.93, 121.66, 113.86, 112.32, 32.64. HRMS (EI-TOF) $m/z$: M$^{\bullet+}$ calculated for [C$_{44}$H$_{32}$N$_6$S]$^{\bullet+}$ 676.2409; found 676.2383; difference −3.80 ppm.

**4,7-Bis(4-(9′*H*-[9,3′:6′,9″-tercarbazol]-9′-yl)phenyl)-2,1,3-benzothiadiazole (4e).** Synthesized according to an altered general reaction A with TCz as the donor, using **3** (0.35 mmol, 156 mg, 1 eq.), [*t*-Bu$_3$PH][BF$_4$] (0.04 mmol, 12 mg, 0.12 eq.), palladium(II)-acetate (0.02 mmol, 4 mg, 0.05 eq.), sodium *tert*-butoxide (0.88 mmol, 84 mg, 2.5 eq.), TCz (0.84 mmol, 419 mg, 2.4 eq.), and toluene (7 mL). Product isolated as a bright yellow powder (245 mg, 55%). $^1$H NMR (400 MHz, CD$_2$Cl$_2$): $\delta$ 8.45 (d, $J$ = 8.5 Hz, 4H), 8.35 (d, $J$ = 2.0 Hz, 4H), 8.18 (d, $J$ = 7.6 Hz, 8H), 8.11 (s, 2H), 8.00 (d, $J$ = 8.5 Hz, 4H), 7.87 (d, $J$ = 8.6 Hz, 4H), 7.70 (dd, $J$ = 8.6, 2.0 Hz, 4H), 7.49–7.40 (m, 16H), 7.30 (ddd, $J$ = 8.0, 6.2, 2.0 Hz, 8H). $^{13}$C{$^1$H} NMR (101 MHz, CD$_2$Cl$_2$): $\delta$ 142.17, 141.03, 137.68, 137.49, 132.98, 132.23, 131.54, 130.87, 128.92, 127.51, 126.64, 126.32, 124.58, 123.50, 120.60, 120.11, 111.92, 111.08, 110.12. HRMS (EI-TOF) $m/z$: M$^{\bullet+}$ calculated for [C$_{90}$H$_{54}$N$_8$S]$^{\bullet+}$ 1278.4192; found 1278.4231; difference 3.02 ppm.

**9,9′-(2,1,3-Benzothiadiazole-4,7-diylbis(4,1-phenylene))bis-(*N*3,*N*3,*N*6,*N*6-tetra-*p*-tolyl-9*H*-carbazole-3,6-diamine) (4f).** Synthesized according to an altered general reaction A with TTCA as the donor, using **3** (0.45 mmol, 200 mg, 1 eq.), [*t*-Bu$_3$PH][BF$_4$] (0.05 mmol, 15 mg, 0.12 eq.), palladium(II)acetate (0.02 mmol, 5 mg, 0.05 eq.), sodium *tert*-butoxide (1.12 mmol, 108 mg, 2.5 eq.), TTCA (1.08 mmol, 600 mg, 2.4 eq.), and toluene (9 mL). The initially isolated solid was further purified by Soxhlet extraction with acetone. Product isolated as a red powder (415 mg, 66%). $^1$H NMR (400 MHz, THF-d$_8$): $\delta$ 8.41 (d, $J$ = 8.6 Hz, 4H), 8.12 (s, 2H), 7.86–7.77 (m, 8H), 7.46 (d, $J$ = 8.7 Hz, 4H), 7.18 (dd, $J$ = 8.8, 2.2 Hz, 4H), 7.01–6.87 (m, 32H), 2.24 (s, 24H). $^{13}$C{$^1$H} NMR (101 MHz, THF-d$_8$): $\delta$ 154.89, 147.28, 142.15, 138.84, 138.64, 131.55, 131.35, 130.13, 128.98, 127.30, 126.16, 125.24, 123.43, 121.56, 118.80, 116.42, 111.37, 20.58. HRMS (EI-TOF) $m/z$: [M + H]$^+$ calculated for [C$_{98}$H$_{78}$N$_8$S + H]$^+$ 1399.6148; found 1399.6009; difference −4.36 ppm.

 

**4,7-Bis(5-(10-methylphenazin-5(10*H*)-yl)thiophen-2-yl)-2,1,3-benzothiadiazole (7).** Synthesized according to an altered general reaction A with MPAZ as the donor and **6** instead of **3**, as follows: **6** (0.98 mmol, 450 mg, 1 eq.), [*t*-$Bu_3PH$][$BF_4$] (0.12 mmol, 34 mg, 0.12 eq.), palladium(II)acetate (0.05 mmol, 11 mg, 0.05 eq.), sodium *tert*-butoxide (2.46 mmol, 236 mg, 2.5 eq.), and MPAZ (2.38 mmol, 463 mg, 2.4 eq.) The reaction was monitored by TLC (4 : 1 hexanes : dichloromethane) until no **6** remained. The initially isolated solid was purified with a silica column (4 : 1 hexanes : dichloromethane). The product was isolated as a dark red solid (87 mg, 13%). $^1$H NMR (400 MHz, DMSO-$d_6$): $\delta$ 8.24 (d, $J$ = 4.0 Hz, 2H), 8.20 (s, 2H), 7.27 (d, $J$ = 4.0 Hz, 2H), 6.81–6.74 (m, 4H), 6.64–6.56 (m, 8H), 6.35–6.27 (m, 4H), 3.05 (s, 6H). $^{13}$C{$^1$H} NMR (101 MHz, DMSO-$d_6$): $\delta$ 144.23, 136.96, 136.79, 131.28, 130.08, 128.14, 125.76, 123.11, 113.71, 111.83, 106.91, 101.45, 90.40, 32.02. HRMS (EI-TOF) $m/z$: $M^{\bullet+}$ calculated for $[C_{40}H_{28}N_6S_3]^{\bullet+}$ 688.1538; found 688.1542; difference 0.63 ppm.

**4,7-Bis(4,4,8,8,12,12-hexamethyl-8,12-dihydro-4*H*-benzo[9,1]-quinolizino[3,4,5,6,7-*defg*]acridin-2-yl)-2,1,3-benzothiadiazole (9).** A 4 mL vial was charged with **8** (0.13 mmol, 50 mg, 1 eq.), HMAT-Br (0.28 mmol, 126 mg, 2.2 eq.), potassium carbonate (0.77 mmol, 107 mg, 6 eq.), and $Pd(PPh_3)_4$ (0.006 mmol, 7.4 mg, 0.05 eq.). The vial was evacuated and back filled with nitrogen gas three times. Separately, a THF/water mixture (2 : 1, 2.1 mL) was sparged with nitrogen gas for 15 min. The THF/water mixture was added *via* air-tight syringe and the reaction was heated with an oil bath set to 80 °C. The reaction was monitored by TLC (10 : 1 hexanes: ethyl acetate) until no **8** remained (approximately 17 h). The reaction was cooled to room temperature and the volatiles removed. The mixture was purified with a silica column (4 : 1 gradient to 3 : 1 hexanes : dichloromethane). The product was isolated as a red solid (15 mg, 23%). $^1$H NMR (400 MHz, $CD_2Cl_2$): $\delta$ 8.14 (s, 4H), 7.90 (s, 2H), 7.48–7.41 (m, 8H), 7.17 (t, $J$ = 7.7 Hz, 4H), 1.75 (s, 24H), 1.65 (s, 12H). $^{13}$C{$^1$H} NMR (101 MHz, $CD_2Cl_2$): $\delta$ 154.83, 132.61, 132.37, 132.07, 132.04, 130.43, 130.40, 130.38, 127.31, 125.15, 124.13, 124.05, 123.54, 36.12, 35.91, 33.64, 33.36. HRMS (FD-TOF) $m/z$: $M^{\bullet+}$ calculated for $[C_{60}H_{54}N_4S]^{\bullet+}$ 862.40692; found 862.40642; difference −0.57 ppm.

### Polymer dot synthesis

**4e**, **f**, or **9** (1.2 mg) and Pluronic F127 (14 mg) were dissolved in 2.4 mL of $CHCl_3$. Volatiles were completely removed *in vacuo*. 1.7 mL of deionized water was then added to 1.2 mg of the obtained solid and the mixture was sonicated for 5 min. This dispersion was then used without any further purification.

## Conflicts of interest

There are no conflicts to declare.

## References

1 G. Niu, R. Zhang, J. P. C. Kwong, J. W. Y. Lam, C. Chen, J. Wang, Y. Chen, X. Feng, R. T. K. Kwok, H. H.-Y. Sung, I. D. Williams, M. R. J. Elsegood, J. Qu, C. Ma, K. S. Wong, X. Yu and B. Z. Tang, *Chem. Mater.*, 2018, **30**, 4778–4787.
2 B. Situ, M. Gao, X. He, S. Li, B. He, F. Guo, C. Kang, S. Liu, L. Yang, M. Jiang, Y. Hu, B. Z. Tang and L. Zheng, *Mater. Horiz.*, 2019, **6**, 546–553.
3 C. Tang, Q. Zheng, H. Zhu, L. Wang, S.-C. Chen, E. Ma and X. Chen, *J. Mater. Chem. C*, 2013, **1**, 1771.
4 T.-C. Lin, Y.-F. Chen, C.-L. Hu and C.-S. Hsu, *J. Mater. Chem.*, 2009, **19**, 7075.
5 J. H. Strickler and W. W. Webb, *Opt. Lett.*, 1991, **16**, 1780.
6 B. H. Cumpston, S. P. Ananthavel, S. Barlow, D. L. Dyer, J. E. Ehrlich, L. L. Erskine, A. A. Heikal, S. M. Kuebler, I.-Y. S. Lee, D. McCord-Maughon, J. Qin, H. Röckel, M. Rumi, X.-L. Wu, S. R. Marder and J. W. Perry, *Nature*, 1999, **398**, 51–54.
7 F. Terenziani, C. Katan, E. Badaeva, S. Tretiak and M. Blanchard-Desce, *Adv. Mater.*, 2008, **20**, 4641–4678.
8 M. Pawlicki, H. A. Collins, R. G. Denning and H. L. Anderson, *Angew. Chem., Int. Ed.*, 2009, **48**, 3244–3266.
9 R. Weissleder, *Nat. Biotechnol.*, 2001, **19**, 316–317.
10 A. M. Smith, M. C. Mancini and S. Nie, *Nat. Nanotechnol.*, 2009, **4**, 710–711.
11 H. M. Kim and B. R. Cho, *Chem. Rev.*, 2015, **115**, 5014–5055.
12 T. He, S. Sreejith, Y. Gao, A. C. Grimsdale, Y. Zhao, X. Lin and H. Sun, *Appl. Phys. Lett.*, 2015, **106**, 111904.
13 T. He, Y. Wang, X. Tian, Y. Gao, X. Zhao, A. C. Grimsdale, X. Lin and H. Sun, *Appl. Phys. Lett.*, 2016, **108**, 011901.
14 K. S. Kim, J. M. Lim, A. Osuka and D. Kim, *J. Photochem. Photobiol., C*, 2008, **9**, 13–28.
15 P. C. Ray and Z. Sainudeen, *J. Phys. Chem. A*, 2006, **110**, 12342–12347.
16 F. Ricci, F. Elisei, P. Foggi, A. Marrocchi, A. Spalletti and B. Carlotti, *J. Phys. Chem. C*, 2016, **120**, 23726–23739.
17 S. Yao, B. Kim, X. Yue, M. Y. Colon Gomez, M. V. Bondar and K. D. Belfield, *ACS Omega*, 2016, **1**, 1149–1156.
18 S. Kato, T. Matsumoto, M. Shigeiwa, H. Gorohmaru, S. Maeda, T. Ishi-i and S. Mataka, *Chem. – Eur. J.*, 2006, **12**, 2303–2317.
19 B. A. D. Neto, A. A. M. Lapis, E. N. da Silva Júnior and J. Dupont, *Eur. J. Org. Chem.*, 2013, 228–255.
20 B. A. D. Neto, P. H. P. R. Carvalho and J. R. Correa, *Acc. Chem. Res.*, 2015, **48**, 1560–1569.
21 F. S. Mancilha, B. A. DaSilveira Neto, A. S. Lopes, P. F. Moreira, F. H. Quina, R. S. Gonçalves and J. Dupont, *Eur. J. Org. Chem.*, 2006, 4924–4933.
22 Y. Wang, M. Chen, N. Alifu, S. Li, W. Qin, A. Qin, B. Z. Tang and J. Qian, *ACS Nano*, 2017, **11**, 10452–10461.
23 W. Qin, P. Zhang, H. Li, J. W. Y. Lam, Y. Cai, R. T. K. Kwok, J. Qian, W. Zheng and B. Z. Tang, *Chem. Sci.*, 2018, **9**, 2705–2710.
24 L. Lu, T. Zheng, Q. Wu, A. M. Schneider, D. Zhao and L. Yu, *Chem. Rev.*, 2015, **115**, 12666–12731.
25 S. Kato, T. Matsumoto, T. Ishi-i, T. Thiemann, M. Shigeiwa, H. Gorohmaru, S. Maeda, Y. Yamashita and S. Mataka, *Chem. Commun.*, 2004, 2342–2343.
26 N. S. Makarov, S. Mukhopadhyay, K. Yesudas, J.-L. Brédas, J. W. Perry, A. Pron, M. Kivala and K. Müllen, *J. Phys. Chem. A*, 2012, **116**, 3781–3793.

27 Z. Fang, T.-L. Teo, L. Cai, Y.-H. Lai, A. Samoc and M. Samoc, *Org. Lett.*, 2009, **11**, 1–4.
28 Z. Fang, X. Zhang, Y. Hing Lai and B. Liu, *Chem. Commun.*, 2009, 920.
29 Z. Fang, R. D. Webster, M. Samoc and Y. H. Lai, *RSC Adv.*, 2013, **3**, 17914–17917.
30 Z. Fang, V. Chellappan, R. D. Webster, L. Ke, T. Zhang, B. Liu and Y.-H. Lai, *J. Mater. Chem.*, 2012, **22**, 15397.
31 H. Sun, C. Zhong and J.-L. Brédas, *J. Chem. Theory Comput.*, 2015, **11**, 3851–3858.
32 L. Kronik, T. Stein, S. Refaely-Abramson and R. Baer, *J. Chem. Theory Comput.*, 2012, **8**, 1515–1531.
33 X.-K. Chen, D. Kim and J.-L. Brédas, *Acc. Chem. Res.*, 2018, **51**, 2215–2224.
34 A. Chantzis, A. D. Laurent, C. Adamo and D. Jacquemin, *J. Chem. Theory Comput.*, 2013, **9**, 4517–4525.
35 J. Mei, N. L. C. Leung, R. T. K. Kwok, J. W. Y. Lam and B. Z. Tang, *Chem. Rev.*, 2015, **115**, 11718–11940.
36 M. K. Etherington, F. Franchello, J. Gibson, T. Northey, J. Santos, J. S. Ward, H. F. Higginbotham, P. Data, A. Kurowska, P. L. Dos Santos, D. R. Graves, A. S. Batsanov, F. B. Dias, M. R. Bryce, T. J. Penfold and A. P. Monkman, *Nat. Commun.*, 2017, **8**, 14987.
37 I. Marghad, F. Bencheikh, C. Wang, S. Manolikakes, A. Rérat, C. Gosmini, D. H. Kim, J.-C. Ribierre and C. Adachi, *RSC Adv.*, 2019, **9**, 4336–4343.
38 R. S. Nobuyasu, J. S. Ward, J. Gibson, B. A. Laidlaw, Z. Ren, P. Data, A. S. Batsanov, T. J. Penfold, M. R. Bryce and F. B. Dias, *J. Mater. Chem. C*, 2019, **7**, 6672–6684.
39 M. K. Etherington, F. Franchello, J. Gibson, T. Northey, J. Santos, J. S. Ward, H. F. Higginbotham, P. Data, A. Kurowska, P. L. Dos Santos, D. R. Graves, A. S. Batsanov, F. B. Dias, M. R. Bryce, T. J. Penfold and A. P. Monkman, *Nat. Commun.*, 2017, **8**, 14987.
40 L. Yao, S. Zhang, R. Wang, W. Li, F. Shen, B. Yang and Y. Ma, *Angew. Chem., Int. Ed.*, 2014, **53**, 2119–2123.
41 N. S. Makarov, M. Drobizhev and A. Rebane, *Opt. Express*, 2008, **16**, 4029.
42 J. Yu, Y. Rong, C.-T. Kuo, X.-H. Zhou and D. T. Chiu, *Anal. Chem.*, 2017, **89**, 42–56.
43 S.-Y. Kuo, H.-H. Li, P.-J. Wu, C.-P. Chen, Y.-C. Huang and Y.-H. Chan, *Anal. Chem.*, 2015, **87**, 4765–4771.
44 M. Massey, M. Wu, E. M. Conroy and W. R. Algar, *Curr. Opin. Biotechnol.*, 2015, **34**, 30–40.
45 N. R. Paisley, C. M. Tonge, E. R. Sauvé, S. V. Halldorson and Z. M. Hudson, *J. Polym. Sci., Part A: Polym. Chem.*, 2018, **56**, 2183–2191.
46 E. Shi, H. Zhuang, Z. Liu, X. Cheng, H. Hu, N. Li, D. Chen, Q. Xu, J. He, H. Li, J. Lu and J. Zheng, *Dyes Pigm.*, 2015, **122**, 66–73.
47 C. Dai, D. Yang, W. Zhang, B. Bao, Y. Cheng and L. Wang, *Polym. Chem.*, 2015, **6**, 3962–3969.
48 Z. Ni, H. Wang, Q. Zhao, J. Zhang, Z. Wei, H. Dong and W. Hu, *Adv. Mater.*, 2019, **31**, 1806010.
49 S. S. Reddy, V. G. Sree, K. Gunasekar, W. Cho, Y.-S. Gal, M. Song, J.-W. Kang and S.-H. Jin, *Adv. Opt. Mater.*, 2016, **4**, 1236–1246.
50 X.-Q. Zhu, Z. Dai, A. Yu, S. Wu and J.-P. Cheng, *J. Phys. Chem. B*, 2008, **112**, 11694–11707.
51 H. Liu, G. Cheng, D. Hu, F. Shen, Y. Lv, G. Sun, B. Yang, P. Lu and Y. Ma, *Adv. Funct. Mater.*, 2012, **22**, 2830–2836.
52 E. R. Sauvé, J. Paeng, S. Yamaguchi and Z. M. Hudson, *J. Org. Chem.*, 2019, DOI: 10.1021/acs.joc.9b02283.
53 Z. Fang, T.-L. Teo, L. Cai, Y.-H. Lai, A. Samoc and M. Samoc, *Org. Lett.*, 2009, **11**, 1–4.
54 G. M. Sheldrick, *Acta Crystallogr., Sect. A: Found. Adv.*, 2015, **71**, 3–8.
55 O. V. Dolomanov, L. J. Bourhis, R. J. Gildea, J. A. K. Howard and H. Puschmann, *J. Appl. Crystallogr.*, 2009, **42**, 339–341.
56 G. M. Sheldrick, *Acta Crystallogr., Sect. C: Struct. Chem.*, 2015, **71**, 3–8.
57 F. Ni, Z. Wu, Z. Zhu, T. Chen, K. Wu, C. Zhong, K. An, D. Wei, D. Ma and C. Yang, *J. Mater. Chem. C*, 2017, **5**, 1363–1368.

 